A reflection zone plate concept for RIXS spectrometry

CHRISTOPH BRAIG[1,*], HEIKE LÖCHEL[1], JENS REHANEK[2], ALEXANDER FIRSOV[1], MARIA BRZHEZINSKAYA[3], AND ALEXEI ERKO[1]

[1] Institut für Nanometeroptik und Technologie, Helmholtz-Zentrum Berlin für Materialien und Energie, 12489 Berlin, Germany
[2] Paul Scherrer Institut, 5232 Villigen, Switzerland
[3] Main Department Scientific-Technical Infrastructure II, Helmholtz-Zentrum Berlin für Materialien und Energie, 12489 Berlin, Germany
[*] Corresponding author: christoph.braig@helmholtz-berlin.de

Compiled December 1, 2016

We simulate a proof-of-principle design of a wavelength dispersive, parallel spectrometer for use in resonant inelastic X-ray scattering (RIXS). The instrument relies on a multiple channel reflection zone plate (RZP) array, enabling the recording of fluorescence spectra from an acceptance angle of (18×19) arcmin^2 with a mainly source size limited resolving power of $(0.2 - 2.6) \times 10^4$ over an energy range of 21 eV at the L-edge of Fe around 715 eV. An optimal two-dimensional signal readout preserves the spectral resolution to a large extent for widely open exit apertures $\gtrsim 50\,\mathrm{mm}^2$. The geometrical parameters are matched to the PEAXIS end station at the BESSY II synchrotron facility and relaxed RZP line densities $< 9 \times 10^2\,\mathrm{mm}^{-1}$ assure the technical feasibility. An error budget estimation with respect to fabrication and alignment tolerances provides the link to real, RZP-based RIXS experiments in future.

OCIS codes: *(050.2770) Gratings; (300.6190) Spectrometers; (340.7480) X-rays, soft x-rays and extreme ultraviolet (EUV).*

http://dx.doi.org/10.1364/ao.XX.XXXXXX

1. INTRODUCTION

During the past two decades [1, 2], elliptical off-axis reflection zone plates (RZPs) have proven successfully as efficient all-in-one diffractive optical elements (DOEs) for soft and hard X-ray imaging, but also in the field of wavelength dispersive spectroscopy, where crystals cannot be applied. Prototypes have been developed [3, 4] and used in various experiments [5–8]. The RZP approach was hence proposed as well [9, 10] for resonant inelastic X-ray scattering (RIXS) [11], whose photon limited detection should provide a spectral resolution of $\sim 10^{-1}$ eV or less for soft X-rays below ~ 1 keV to measure excitations such as magnons or the phonon band [12]. Conventional grating spectrometers, which are being mostly used so far, typically consist of 3 optical elements, namely the primary entrance mirror, the grating and a refocusing mirror. The total transmission scales accordingly with the 3$^{\mathrm{rd}}$ power of the already moderate surface reflectivity for serial arrangements of that kind. Their integration into a single DOE will hence clearly enhance the signal flux and so the sensitivity, despite an albeit similar vertical acceptance angle as in the traditional configuration. To match the horizontal one, several RZPs can be assembled in parallel [4–6].

The recent application of such an RZP array (RZPA) to analyze K_α emission lines, as produced by low-Z elements from Li to Ga and some of their compounds [13], established parallel spectrometry using multiple energy channels, covering the desired bandwidth, as an elegant and powerful method for stationary RIXS experiments, e.g. at synchrotron radiation facilities. Based on this initial work, the present paper aims to improve the performance in terms of resolution and sensitivity, demonstrated by means of a theoretical study and numerical simulations on an optimized and feasible instrumental sample design for measurements of the Fe $L_{2/3}$-edge around 715 eV at the BESSY II PEAXIS end station [10]. The setup is developed in Sect. 2. Its optical properties are investigated in Sect. 3, followed by an error budget estimation in Sect. 4 and concluded with the key characteristics in Sect. 5.

2. INSTRUMENTAL DESIGN

We consider an X-ray reflection grating setup as shown in Fig. 1, designed for simultaneous, broadband fluorescence spectrometry without any moving parts. The DOE is operated under grazing incidence in an off-axis region $X_2 \leq x \leq X_1$ to select the $(-1)^{\mathrm{st}}$ diffraction order, avoiding specular reflection from the optical center $\vec{r} = 0$. The source emission at $\vec{R}_1$ is deflected from the plane substrate in $z = 0$ and the dispersed pattern is observed along the focal line of width w_{det}, defined as $\tilde{y} \equiv \vec{R}_2 + \mathcal{D}(x)\, y\, \vec{e}_y$. Here we used $\vec{R}_i = R_i\,(\mp\cos\theta, 0, \sin\theta)^T$ and $\mathcal{D}(x) \equiv (x + R_1\cos\theta)^{-1}\cos\theta(R_1 + R_2)$, by means of the convention that the upper (lower) sign in "$\mp$" is associated with the subscript 1 (2), respectively. In agreement with this notation and for convenience, we will refer to the local coordinate system of the detector via $\vec{r}_{\mathrm{det}} \equiv (\tilde{x}, \tilde{y})^T$, where applicable.

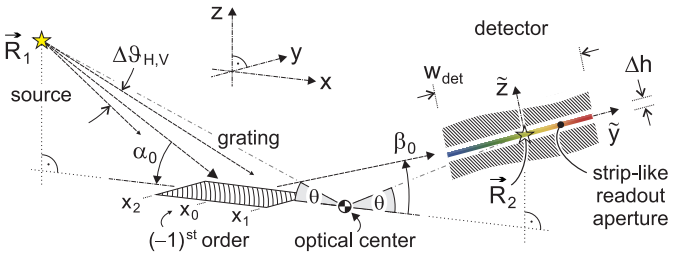

Fig. 1. Wavelength dispersive parallel spectroscopy by an off-axis RZPA; the notation is adopted from [4]. Source and image are located at $\vec{R}_1$ and around $\vec{R}_2$, respectively. The intensity distribution is recorded on the detector and analyzed from a narrow region of dimensions $w_{det} \times \Delta h$ near the $\tilde{y}$-axis.

Following the "wavelength separator" made of fanned out single RZPs [4], we equip the array now with N channels for successive energies E_n $(1 \leq n \leq N)$ around their mean $E_0 = \sqrt{E_{min} E_{max}}$. A constant spacing $|E_{n\pm1} - E_n| = \Delta E_n / N$ is assumed, such that the total covered band is given by $\Delta E_n = E_{max} - E_{min}$. Using the Planck constant h and the speed of light c, the demand of an energy-independent [6] resolving power $\mathcal{R} \equiv E/\Delta E$ across the RZPA leads to

$$E_n(\vartheta_H) = E_0 \exp[w_{det}^{-1}(R_1 + R_2) \ln(E_{min}/E_{max}) \tan\vartheta_H]. \quad \textbf{(1)}$$

The horizontal (H) component within the solid angle $\Delta\vartheta_H \times \Delta\vartheta_V = (18 \times 19)\,\mathrm{arcmin}^2$ from Fig. 1, given as the discrete inverse function $\vartheta_H(E_n)$ in Eq. (1), determines the orientation via the rotary matrix $\mathbf{M}_n$ and the optical center position $\vec{r}_n^{\star}$ of the n^{th} RZP. Its local coordinates are expressed as $\hat{\vec{r}}_n = \mathbf{M}_n[\vec{r} - \vec{r}_n^{\star}]$. We introduce the abbreviation $\hat{\mathcal{H}}^{(i)}_{\pm,n}(\vec{r}) \equiv \hat{x}_n(\vec{r}) \pm R^{\star}_{i,n} \cos\theta^{\star}_n$, where $R^{\star}_{i,n}$ indicates the entrance and exit arm length with respect to $\vec{r}_n^{\star}$ and $\theta^{\star}_n \approx \theta$ denotes the slightly varying grazing angle. The vector field of the n^{th} channel for λ_n follows as [4]

$$\hat{\vec{g}}_n(\vec{r}) = \sum_{i=1}^{2} \frac{\hat{y}_n(\vec{r})\,\vec{\nabla}_{x,y}\hat{y}_n(\vec{r}) + \hat{\mathcal{H}}^{(i)}_{\pm,n}(\vec{r})\,\vec{\nabla}_{x,y}\hat{x}_n(\vec{r})}{\lambda_n \sqrt{[\hat{y}_n(\vec{r})]^2 + [\hat{\mathcal{H}}^{(i)}_{\pm,n}(\vec{r})]^2 + [R_i \sin\theta]^2}}. \quad \textbf{(2)}$$

Their set union $\bigcup_n \hat{\vec{g}}_n(\vec{r})$ is then ray traced for key data which are specified in Tab. 1 to match the instrumental needs [4, 10]. As defined previously [4, 7], the geometrical pathways $R'_{1,2}$ as

Table 1. Design parameters for the multiple channel RZPA

ΔE_n [eV]	R'_1 [mm]	R'_2 [mm]	α_0	β_0	L [mm]
21	760	4140	3.0°	0.427°	80
E_0 [eV]	R_1 [mm]	R_2 [mm]	θ		X_0 [mm]
714.923	2759.25	2140.11	0.826°		−2000

well as incidence (α_0) and exit (β_0) angles refer to the off-axis grating position at $\vec{r} = (X_0, 0, 0)^T$ in Fig. 1, rather than the optical midpoint $\vec{r} = 0$. Across its mean width of ≈ 4 mm, the overall array provides $N = 21$ equidistant energy channels E_n between 705 eV and 725 eV. Figure 2 shows a zoomed cutout of this nearly rectangular albeit slightly trapezoidal grating shape of length $L = |X_2 - X_1|$ with $X_{1,2} = X_0 \pm L/2$ (Tab. 1).

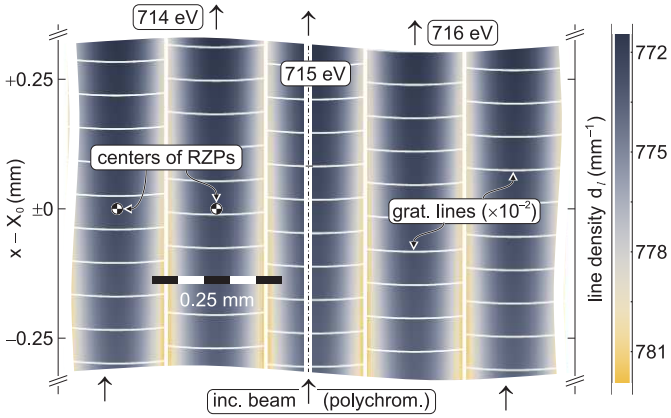

Fig. 2. Central region around X_0 of the fanned out RZPA in top view for the parameters from Tab. 1. Every 100th grating groove of the innermost 5 RZPs is drawn to scale (white arcs). Geometrical center positions of the 9th and 10th RZP are depicted exemplarily; the dash-dotted line represents the x-axis. The source illuminates each channel equally, from the bottom in the plot. The line density d_l is color-coded on the right.

For reasons of simplicity and to minimize reflection losses, the detector is inclined to normal incidence with respect to the beam direction, given by the exit angle β_0. The CCD camera itself (ANDOR iKon-L 936) features 2048×2048 pixel with an edge length $\Delta w^{(geo)}_{pixel} = 13.5\,\mu$m, providing a net detector width $w_{det} = 26$ mm – the outermost 0.8 mm on each side of the full field of $(27.6 \times 27.6)\,\mathrm{mm}^2$ are reserved to align the device.

The spectral image pattern can be captured and recorded from the full-sized detector without any slit. A comparative study of Figs. 1 and 2, together with the 2D imaging camera in particular, reveals the working principle of our instrument, which differs from more conventional spectrometers that only separate in one, i.e. the $\tilde{z}$-direction. Instead, an Fe $L_{2/3}$ edge spectrum will be dispersed in two dimensions. In the first instance, we consider the vertical dispersion by each single RZP with a superior resolution for photons near any one of the design energies E_n. The chromatic aberration [7, 8, 14] nonetheless constrains the free spectral range (FSR) to $\lesssim 1$ eV (FWHM) around E_n – and hence also the usable readout aperture for the reconstruction of the spectrum to a relatively narrow, strip-like region of width Δh, as colorized ("rainbow") in Fig. 1. The key to an enlarged FSR, namely the energy sorted arrangement of these RZPs to an array, leads to an effective dispersion along the horizontal $\tilde{y}$-axis of the detector, too. Due to their well matched spacing by 1 eV, the RZP channels act as "pre-selectors" for the photons and allow to keep a good, constant resolving power over the desired band of 21 eV, as elaborated in Sect. 3.

3. OPTICAL PERFORMANCE

The rectangular, flat source is modeled as a uniform spatial distribution of incoherently assembled point emitters for N energies E_n. We would expect a vertical (V) focal spot size near $\varnothing^{(V)}_{foc.}(E_n) = M \frac{\sin\alpha_0}{\sin\beta_0} \sqrt{[\varnothing^{(V)}_{src.}]^2 + [E_n^{-1} hc/\vartheta_V]^2}$ with $M \equiv R'_2/R'_1$ [7] and similarly $\varnothing^{(H)}_{foc.}(E_n) = M\sqrt{[\varnothing^{(H)}_{src.}]^2 + [N E_n^{-1} hc/\vartheta_H]^2}$ in the lateral direction (H). Besides however, a Gaussian pixel blur $\Delta w^{(eff)}_{pixel} = r_s \times \Delta w^{(geo)}_{pixel}$ of the CCD array, due to split events with $1 \leq r_s \leq 3$, will usually degrade the actual resolution.

For a source size of $(10 \times 3)\,\mu\mathrm{m}^2$, we obtain at the mean energy of 715 eV the monochromatic footprint in Fig. 3. From the

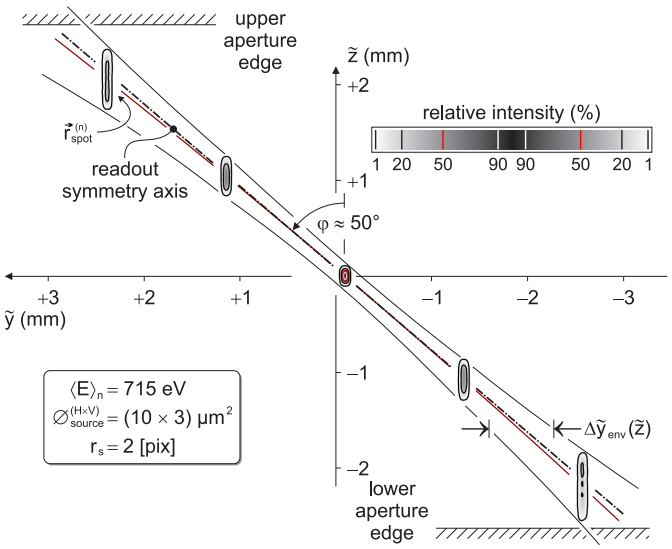

Fig. 3. Discrete pattern, ray traced and convolved with the diffractive point spread function for the configuration as defined in the inset box. Here, the exit aperture selects the spots generated by 5 adjacent RZPs, i.e. the innermost channels depicted in Fig. 2. The peaks lie on the curved, dark red line, which is approximated by the straight but inclined, dash-dotted symmetry axis of their envelope (curved solid lines).

full detector area, the sufficiently narrow region in the vicinity of the $\tilde{y}$-axis accepts a number of blurred spots, depending on the aperture width $\Delta h \lesssim 5\,\mathrm{mm}$. Their peak position $\vec{r}^{\,(n)}_{\mathrm{spot}}$, measured in local detector coordinates, follows the curved line in Fig. 3. In good agreement with an analytical model based on the nonlinear grating equation – the averaged standard error over the range $|\tilde{y}| \leq w_{\mathrm{det}}/2$ amounts to ±3% – the numerical simulation results can be described by $d\tilde{z}^{(n)}_{\mathrm{spot}}/d\tilde{y} \approx \cot\varphi + \sum_{k=1}^{2} c_k [\tilde{y}^{(n)}_{\mathrm{spot}}]^k$ with $c_1 = -2.6 \times 10^{-2}\,\mathrm{mm}^{-1}$ and $c_2 = 8.3 \times 10^{-4}\,\mathrm{mm}^{-2}$. For convenience, we approximate the function $\tilde{z}^{(n)}_{\mathrm{spot}}(\tilde{y})$ by the straight but slanted symmetry axis, along which the signal is readout. The slight deviation $\delta\tilde{z}^{(n)}_{\mathrm{spot}} \leq 0.1\,\mathrm{mm}$ near $|\tilde{y}|$ from the exact curve is visible in the asymmetric intensity distribution in Fig. 3, where especially the outermost spots are off-centered from the dash-dotted line. Beyond the strip-like aperture, $\varnothing^{(V)}_{\mathrm{foc.}}$ spreads more and more, due to zone plate aberrations. The chromatic imaging error dominates [7, 8] by at least (99 : 1)% above coma, astigmatism and field curvature [2, 14], which are nevertheless also inherently incorporated in the ray tracing code [4].

The lateral (H) and vertical (V) dispersion terms $\partial_{\tilde{y},\tilde{z}} E|_{\tilde{z}=0}$ are hence related via $\tan\varphi \approx 1.19$, determined by the instrumental design (Tab. 1). Since our RZPA records a continuous spectrum over 21 eV rather than fluorescence from distinct elements or chemical compounds [6, 13], the effective resolving power depends on the horizontal width $\Delta\tilde{y}_{\mathrm{env}}(\tilde{z})$ of the envelope on the blurred spots in Fig. 3. Toward the focal line $\tilde{z} \approx 0$, the waist and highest value $\mathcal{R}_{\Delta h\to 0}$ is reached and follows as the lower one ("⇋") of the perpendicular components $\mathcal{R}^{(0)}_{\mathrm{H,V}}$ [7],

$$\mathcal{R}_{\Delta h\to 0} = \min_{\mathrm{H}\rightleftharpoons\mathrm{V}}\{\mathcal{R}^{(0)}_{\mathrm{H,V}} \equiv \left[\partial_{\tilde{y},\tilde{z}} E|_{\tilde{z}=0} \times \varnothing^{(\mathrm{H,V})}_{\mathrm{focus}}(E_n)\right]^{-1} E_n\}. \quad \textbf{(3)}$$

While the diffraction limited horizontal focus width for discrete channel energies expands with N, the vertical dimension of the spot does not; and for an assumed reference source size around $(4.3 \times 1.0)\,\mu\mathrm{m}^2$ the choice of $N = 21$ nearly equals the (H) and (V) components in Eq. (3), due to $\varnothing^{(\mathrm{H})}_{\mathrm{foc.}}(E_n) \approx \tan\varphi \times \varnothing^{(\mathrm{V})}_{\mathrm{foc.}}(E_n)$.

Across the narrow band ΔE_c, the function $\Delta\tilde{y}_{\mathrm{env}}(\tilde{z})$ varies only along $\tilde{z}$, but holds for every energy with a tolerance of few %. The mean, effective breadth of the envelope as the continuous extension of the discrete intensity pattern in Fig. 3 is computed via numerical integration [8], to evaluate the function

$$\mathcal{R}(\Delta h) = \partial_{\tilde{y}} E|_{\tilde{z}=0} \times \langle \Delta\tilde{y}_{\mathrm{env}}(\tilde{z})\rangle_{\tilde{z}}, \quad \text{where} \quad |\tilde{z}| \leq \Delta h/2. \quad \textbf{(4)}$$

Simulations reveal a relatively weak correlation between $\mathcal{R}$ and $\varnothing^{(\mathrm{H})}_{\mathrm{src.}} \sim \mu\mathrm{m}$, in contrast to the critical impact of the other dimension $\varnothing^{(\mathrm{V})}_{\mathrm{src.}}$. We present accordingly results for the standard low resolution (LR) and a currently hypothetical high resolution (HR) regime as specified in Fig. 4. In the asymptotic "large

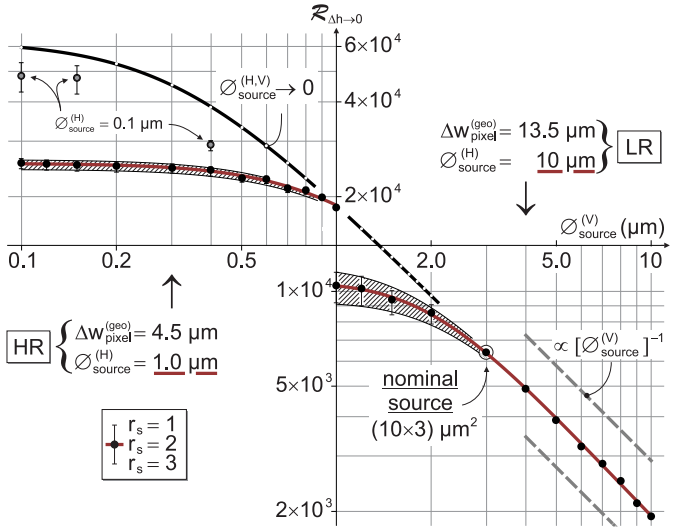

Fig. 4. Maximal resolving power $\mathcal{R}_{\Delta h\to 0}$ for $\varnothing^{(\mathrm{V})}_{\mathrm{src.}} \lesssim 1\,\mu\mathrm{m}$ in the HR and LR regime, respectively, with fixed conditions for $\Delta w^{(\mathrm{geo})}_{\mathrm{pixel}}$ and $\varnothing^{(\mathrm{H})}_{\mathrm{src.}}$ in each case. Error bars and hatched regions mark the variability due to split events $(1 \leq r_s \leq 3)$. The black solid line refers to an ideal point source, i.e. $\varnothing^{(\mathrm{H,V})}_{\mathrm{source}} \to 0$.

source" limit $\varnothing^{(\mathrm{H,V})}_{\mathrm{source}} \sim 10\,\mu\mathrm{m}$, geometrical imaging dominates over diffraction, leading to the linear decline $\mathcal{R}_{\Delta h\to 0} \propto 1/\varnothing^{(\mathrm{V})}_{\mathrm{src.}}$. Toward smaller source dimensions $\varnothing^{(\mathrm{V})}_{\mathrm{src.}} \sim 1\,\mu\mathrm{m}$, the CCD confines the resolving power to $\approx 1 \times 10^4$ – mainly by the pixel size $\Delta w^{(\mathrm{geo})}_{\mathrm{pixel}}$, but to a minor degree also by the electronic blur r_s. Sophisticated image processing could yield a 3× better spatial resolution [15], to benefit from "nano source" beamlines with $\varnothing^{(\mathrm{H,V})}_{\mathrm{source}} < 1\,\mu\mathrm{m}$ in the HR domain. Today's and upcoming focusing optics might allow at best for $\mathcal{R}_{\Delta h\to 0} \lesssim 3 \times 10^4$, enabled by $\varnothing^{(\mathrm{H})}_{\mathrm{src.}} \times \varnothing^{(\mathrm{V})}_{\mathrm{src.}} \lesssim 10^{-1}\,\mu\mathrm{m}^2$ and even excelled for a cross-sectional area of $10^{-2}\,\mu\mathrm{m}^2$ or below, as indicated exemplarily in Fig. 4. Diffraction would set nonetheless the upper bound to 6.2×10^4.

Existing beamline optics often favor easily accomplished 1D focusing, yielding source cross sections characterized by $\varnothing^{(\mathrm{V})}_{\mathrm{src.}}/\varnothing^{(\mathrm{H})}_{\mathrm{src.}} \ll 1$. Table 2 lists $\mathcal{R}_{\Delta h\to 0}$ for respective aspect ratios down to 1/49 in the LR domain and basically assuming $r_s = 2$, noted with margins where the simulation reveals significant deviations for $r_s = 3$ (subscript) and $r_s = 1$ (superscript). The partially discontinuous variation of $\mathcal{R}_{\Delta h\to 0}$ with $\varnothing^{(\mathrm{H})}_{\mathrm{src.}}$ reflects statistical ray tracing uncertainties. As the data set in Tab. 2 reveals,

Table 2. Wide-source resolving power $(\times 10^3)$ for $r_s \leq 3$ (LR)

$\varnothing^{(H,V)}_{source}$	19 μm	25 μm	31 μm	37 μm	49 μm
1 μm	$8.04^{+0.3}_{-0.5}$	$6.45^{+0.1}_{-0.2}$	5.52	4.37	3.53
4 μm	$4.99^{+0.1}_{-0.1}$	$4.57^{\pm 0.0}_{-0.1}$	4.25	4.14	3.26
7 μm	$2.73^{\pm 0.0}_{\pm 0.0}$	$2.76^{\pm 0.0}_{\pm 0.0}$	2.85	2.80	3.02
10 μm	$1.93^{\pm 0.0}_{\pm 0.0}$	$1.98^{\pm 0.0}_{\pm 0.0}$	2.04	2.02	1.90

the magnitude of $\varnothing^{(H)}_{src.}$ affects the spectrometric capabilities significantly only for $\varnothing^{(V)}_{src.} \lesssim 4\,\mu$m, whereas toward vertical diameters near 10 μm, even a horizontal source extension up to 49 μm maintains the resolving power of 2×10^3. In analogy, the line source case is also studied in the HR regime, now for scaled down (H) and (V) dimensions. In Tab. 3, the same sub-/superscript notation as above is used. The limit $\mathcal{R}_{\Delta h \to 0}$ is evaluated again in

Table 3. Wide-source resolving power $(\times 10^3)$ for $r_s \leq 3$ (HR)

$\varnothing^{(H,V)}_{source}$	1.9 μm	2.5 μm	3.1 μm	3.7 μm	4.9 μm
0.1 μm	37.5^{+2}_{-3}	30.5^{+1}_{-1}	30.0^{+1}_{-1}	28.8^{+1}_{-1}	27.1^{+1}_{-1}
0.4 μm	29.2^{+1}_{-1}	28.2^{+1}_{-1}	27.8^{+1}_{-1}	27.3^{+1}_{-1}	$24.8^{\pm 0}_{-1}$
0.7 μm	24.5^{+1}_{-1}	24.1^{+1}_{-1}	25.0^{+1}_{-1}	$22.9^{\pm 0}_{-1}$	$22.0^{\pm 0}_{-1}$
1.0 μm	$18.4^{\pm 0}_{\pm 0}$	$19.3^{\pm 0}_{\pm 0}$	$18.6^{\pm 0}_{\pm 0}$	$19.6^{\pm 0}_{\pm 0}$	$18.7^{\pm 0}_{\pm 0}$

the absence of fabrication and alignment errors, but based on $\Delta w^{(eff)}_{pixel} = 4.5\,\mu\text{m} \times r_s$. Obviously, $\varnothing^{(V)}_{src.} \lesssim 0.4\,\mu$m is required to access $\mathcal{R}_{\Delta h \to 0} \gtrsim 3 \times 10^4$. In other words, the more specific source area cross-section $\varnothing^{(H)}_{src.} \times \varnothing^{(V)}_{src.} \lesssim 1.0\,\mu\text{m}^2$ sets here the borderline to that high performance domain, providing $\Delta E \leq 24$ meV.

So far, we have studied the influence of the source size on the resolving power at its upper bound with respect to the aperture width via $\lim_{\tilde{z} \to 0} \langle \Delta \tilde{y}_{env}(\tilde{z}) \rangle_{\tilde{z}}$ in Eq. (4). Remarkably, the readout scheme along the slanted symmetry axis of the diffraction pattern in Fig. 3, inclined to $\varphi \approx 50°$ with respect to the $\tilde{z}$-axis, allows to nearly preserve the limit $\mathcal{R}_{\Delta h \to 0}$ even for a widely open exit aperture, since $\Delta \tilde{y}_{env}(\tilde{z})$ broadens weakly with $|\tilde{z}|$. On the other hand, the recorded count rate grows linearly with Δh. Hence, we predict a strongly enhanced signal-to-noise ratio, in comparison to the alternative spectrum reconstruction which is based on an integration of the pixel entries along the $\tilde{z}$-axis [6]. In Fig. 5, this quintessence of our work and advantage of major relevance for the "photon hungry" RIXS technique is visualized in a two-fold way: We begin with the general relation $\mathcal{R}(\Delta h)$, which is – assembled from 360 simulation runs – represented in colors for various source parameters under LR and HR conditions. On the abscissa, the vertical source size is considered between 0.1 μm and 1.0 μm as usually. Along the ordinate, the exit aperture is for this plot opened on the μm scale in the HR and up to 2.2 mm in the LR regime. As expected, $\mathcal{R}(\Delta h)$ decreases both with $\varnothing^{(V)}_{src.}$ and Δh. In a second step, we fix the source dimension $\varnothing^{(V)}_{src.}$, consider the decline of $\mathcal{R}$ with Δh and determine the ratio $\mathcal{R}/\mathcal{R}_{\Delta h \to 0}$ for this specific source: In both domains (LR/HR), boundaries indicate the regions that ensure a resolving power greater than 95% or 80% of the maximum when the exit aperture is nearly "closed". For instance, an aperture width $\Delta h = 0.1$ mm provides for a source of $(1.0 \times 0.4)\ \mu\text{m}^2$ in

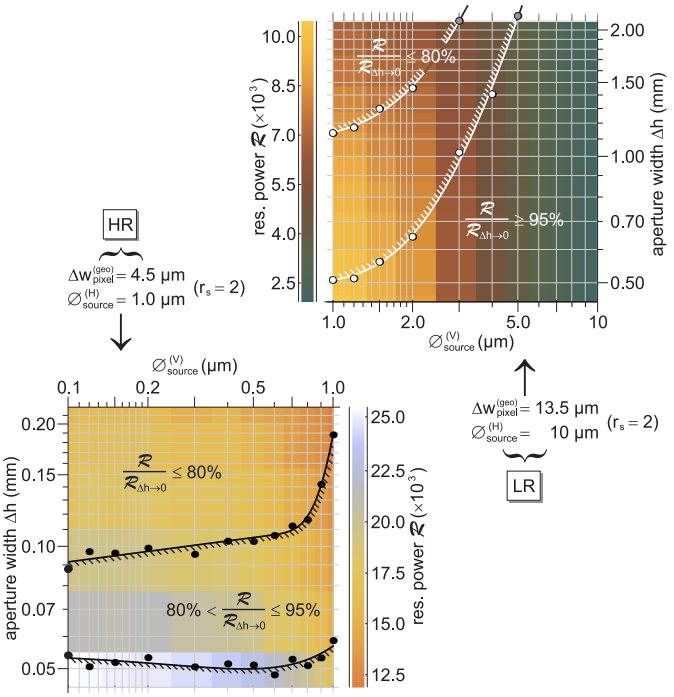

Fig. 5. Aperture width dependence of $\mathcal{R}$ on Δh for a given source size component $\varnothing^{(V)}_{src.}$, color-coded in the LR and HR regime with $r_s = 2$ (see Fig. 4). Hatched contours in white (LR) and black (HR) indicate the degradation of $\mathcal{R}(\Delta h)$ to the 95% and 80% level, relative to the upper bound $\mathcal{R}_{\Delta h \to 0}$ for $\varnothing^{(V)}_{src.}$.

size still 80% of the limit $\mathcal{R}_{\Delta h \to 0} = (2.4 \pm 0.1) \times 10^4$ from Fig. 4; or the signal may be readout from $|\tilde{z}| \leq 0.5$ mm to keep at least 95% of the optimum for an enlarged source of $(10 \times 3)\ \mu\text{m}^2$.

4. ERROR BUDGET

Grating substrate imperfections, expressed as its slope error (rms), provoke a source size dependent and anisotropic effect on the spectrometer performance, as Fig. 6 illustrates. The "large

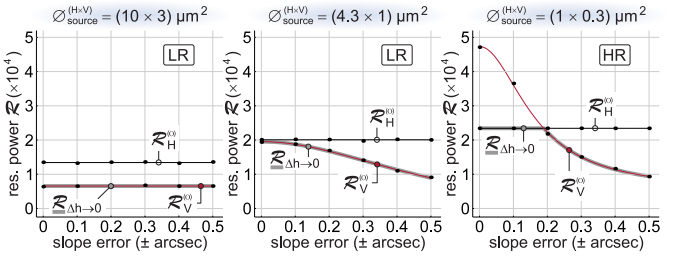

Fig. 6. Influence of the substrate slope error (rms) on the horizontal (black) and vertical (red) components $\mathcal{R}^{(0)}_{H,V}$ from which the actual, usable resolving power $\mathcal{R}_{\Delta h \to 0}$ follows as their minimum (thick gray line), see Eq. (3) for details. Three typical sample sources $\varnothing^{(H,V)}_{source}$ in the LR and HR regime are selected.

source" configuration in the leftmost plot is entirely limited by the vertical (V) contribution to the measurable resolving power $\mathcal{R}_{\Delta h \to 0}$ and tolerates even ± 0.5 arcsec without any losses. For the balanced case with $\varnothing^{(H,V)}_{source} = (4.3 \times 1)\ \mu\text{m}^2$, an at most 20% loss relative to the perfectly smooth sample is expected up to

± 0.2 arcsec – still feasible for sufficiently thick Si wafers of the required size. This estimation on the roughness tolerance holds in the HR regime on the right in Fig. 6 as well, where now the more and more blurred component $\varnothing_{\text{foc.}}^{(\text{V})}$ leads to a rapid decline of the vertical resolution and defines the critical transition $\min_{\text{H}\rightleftharpoons\text{V}}\{\mathcal{R}_{\text{H,V}}^{(0)}\}$ in Eq. (3) near ± 0.2 arcsec.

Typical alignment inaccuracies may manifest themselves in a jitter of the fluorescent region. Now in absence of any substrate roughness, we consider a positional uncertainty of the form $\vec{R}_1 \mapsto \vec{R}_1 \pm \eta\, \mathcal{G}_{\text{FWHM}}\left[\varnothing_{\text{src.}}^{(\text{V})}\right]\vec{e}_z$ with $\eta \geq 0$, modeled by the Gaussian FWHM equivalent $\mathcal{G}_{\text{FWHM}}\left[.\right]$ of the vertical source dimension. In the LR domain, represented by the same two sample sources as in Fig. 6, relative variations $\eta_{\text{LR}} \lesssim \pm 0.4$ keep at least 80% of $\mathcal{R}_{\Delta h \to 0}$, corresponding to an absolute tolerance of $\pm 0.4\,\mu$m and $\pm 1.3\,\mu$m, respectively. Since the lateral (H) focal width rather sets the $\min_{\text{H}\rightleftharpoons\text{V}}\{\mathcal{R}_{\text{H,V}}^{(0)}\}$ in the HR regime for $\varnothing_{\text{src.}}^{(\text{V})} = 0.3\,\mu$m, we estimate $\eta_{\text{HR}} \lesssim \pm 1.3$, leading to the same allowed jitter of $\pm 0.4\,\mu$m to hold the 80% level for this source.

5. CONCLUSION

The proposed spectrometer for transition metal L-edge RIXS combines high sensitivity, enabled by 2D dispersion across a CCD and wide exit aperture readout, with the flexibility of two alternative domains of operation: Determined by the fluorescent source area of a few $(0.1 - 10)\,\mu\text{m}^2$ and the effective pixel size of $(4.5 - 40)\,\mu$m, the instrument yields a resolving power $E/\Delta E \lesssim 1 \times 10^4$ in the standard mode or an even $(2 - 3)\times$ improved performance in the "high resolution" regime.

If the detector surface would be oriented toward the focal line tangent, i.e. inclined to a positive angle approaching $90° - \theta$ with respect to the z-axis in Fig. 1 instead of $-\beta_0$ as assumed in this work, the resolving power could be increased even more in principle [10, 16]. Nonetheless, both source and pixel size should match this modified design, to exploit its potential.

Another possible instrumental variation relies on an analogous array of transmission zone plates (TZPs), whose parameters correspond to the key data of the RZPA from Tab. 1. The transformation between both versions is equivalent to a rotation of the grating plane by an angle $\theta - 90°$ around the optical center [2], such that the source illuminates the off-axis TZP segments in nearly normal incidence from a distance around 2.8 m. Across the radial segment length of 15 mm with a zone width of 123 ± 13 nm, the same number of lines and hence theoretical resolving power $(E/\Delta E)_{\text{max}} = 6.2 \times 10^4$ as well as acceptance solid angle of (18×19) arcmin^2 are provided. Despite its tolerance against misalignment and fabrication inaccuracies, the large-scale, necessarily thin and nanostructured TZP aperture would constitute an advanced technological challenge – clearly surpassed by plane reflective gratings with grooves of 640 ± 70 nm in width, etched into the surface of a Si substrate. In general, the RZP concept enables a much better resolution for the same line density than the TZP approach, but suffers from more serious imaging errors like geometrical aberrations [2, 14].

Our definitely feasible and aberration-reduced demonstrator is therefore based on a multi-energy array of 21 reflection zone plates cut in their $(-1)^{\text{st}}$ diffraction order, covering a bandwidth of 21 eV around 715 eV. Length scales and deflection angles fit to the PEAXIS station at the storage ring BESSY II. All components are commercially available or can be manufactured easily. Fabrication and alignment errors such as substrate imperfections or a source height jitter permit a tolerance of ± 0.2 arcsec (rms) and at least $\pm 40\%$ of the vertical source size.

FUNDING INFORMATION

Support from the BMBF project "Next generation instrumentation for ultrafast X-ray science at accelerator-driven photon sources" (no. 05K12CB4) and a Marie Curie FP7-Reintegration-Grants within the 7th European Community Framework Program (no. PCIG10-GA-2011-297905) is kindly acknowledged.

REFERENCES

1. T. Wilhein, D. Hambach, B. Niemann, M. Berglund, L. Rymell, and H. M. Hertz, "Off-axis reflection zone plate for quantitative soft X-ray source characterization," Appl. Phys. Lett. **71**, 190–192 (1997).
2. A. G. Michette, S. J. Pfauntsch, A. Erko, A. Firsov, and A. Svintsov, "Nanometer focusing of X-rays with modified reflection zone plates," Opt. Commun. **245**, 249–253 (2005).
3. M. Kalläne, J. Buck, S. Harm, R. Seemann, K. Rossnagel, and L. Kipp, "Focusing light with a reflection photon sieve," Opt. Lett. **36**, 2405–2407 (2011).
4. C. Braig, H. Löchel, R. Mitzner, W. Quevedo, P. Loukas, M. Kubin, C. Weniger, A. Firsov, J. Rehanek, M. Brzhezinskaya, P. Wernet, A. Föhlisch, and A. Erko, "Design and optimization of a parallel spectrometer for ultra-fast X-ray science," Opt. Express **22**, 12583–12602 (2014).
5. A. Erko, A. Firsov, and F. Senf, "Novel parallel vacuum ultra-violet / X-ray fluorescence spectrometer," Spectrochimica Acta B **67**, 57–63 (2012).
6. A. Erko, A. Firsov, R. Gubzhokov, A. Bjeoumikhov, A. Günther, N. Langhoff, M. Bretschneider, Y. Höhn, and R. Wedell, "New parallel wavelength-dispersive spectrometer based on scanning electron microscope," Opt. Express **22**, 16897–16902 (2014).
7. H. Löchel, C. Braig, M. Brzhezinskaya, F. Siewert, P. Baumgärtel, A. Firsov, and A. Erko, "Femtosecond high-resolution hard X-ray spectroscopy using reflection zone plates," Opt. Express **23**, 8788–8799 (2015).
8. C. Braig, H. Löchel, A. Firsov, M. Brzhezinskaya, A. Hafner, J. Rehanek, M. Wojcik, A. Macrander, L. Assoufid, and A. Erko, "Hard x-ray spectroscopy and imaging by a reflection zone plate in the presence of astigmatism," Opt. Lett. **41**, 29–32 (2016).
9. J. Rehanek, F. Schäfers, H. Löchel, A. Firsov, J. Grünert, W. Freund, C. Ozkan, S. Molodtsov, and A. Erko, "A case study of novel X-ray Optics for FEL sources," J. Phys. Conf. Series **425**, 052013 (2013).
10. K. Lieutenant, T. Hofmann, C. Schulz, M. V. Yablonskikh, K. Habicht, and E. F. Aziz, "Design concept of the high-resolution end-station PEAXIS at BESSY II: Wide-Q-range RIXS and XPS measurements on solids, solutions, and interfaces," J. Electron Spectroscopy Relat. Phenom. **210**, 54–65 (2016).
11. V. N. Strocov, "Concept of a spectrometer for resonant inelastic X-ray scattering with parallel detection in incoming and outgoing photon energies," J. Synchrotron Rad. **17**, 103–106 (2010).
12. L. J. P. Ament, M. van Veenendaal, T. P. Devereaux, J. P. Hill, and J. van den Brink, "Resonant inelastic x-ray scattering studies of elementary excitations," Rev. Mod. Phys. **83**, 705–767 (2011).
13. A. Hafner, L. Anklamm, A. Firsov, A. Firsov, H. Löchel, A. Sokolov, R. Gubzhokov, and A. Erko, "Reflection zone plate wavelength-dispersive spectrometer for ultra-light elements measurements," Opt. Express **23**, 29476–29483 (2015).
14. M. Young, "Zone Plates and Their Aberrations," J. Opt. Soc. Am. **62** 972–976 (1972).
15. M. R. Soman, D. J. Hall, J. H. Tutt, N. J. Murray, A. D. Holland, T. Schmitt, J. Raabe, and B. Schmitt, "Developing a CCD camera with high spatial resolution for RIXS in the soft X-ray range," Nucl. Instr. Meth. Phys. Res. A **731**, 47—52 (2013).
16. G. Ghiringhelli, A. Piazzalunga, C. Dallera, G. Trezzi, L. Braicovich, T. Schmitt, V. N. Strocov, R. Betemps, L. Patthey, X. Wang, and M. Grioni, "SAXES, a high resolution spectrometer for resonant x-ray emission in the 400–1600 eV energy range," Rev. Sci. Instr. **77**, 113108 (2006).